

ACKNOWLEDGMENTS

We acknowledge funding from the U.S. Army Research Office Award (W911NF-15-1-0152) that enabled the design, modeling, and topological charge characterization of the EP-based OAM laser, Department of Energy Award (DE-SC0014485) that was used to perform the analysis and characterization of the spectral properties of OAM lasing,

and National Science Foundation Award (DMR-1506884) that facilitated the fabrication of the device and optimization of the EP modulation.

SUPPLEMENTARY MATERIALS

www.sciencemag.org/content/353/6298/464/suppl/DC1
Supplementary Text

Figs. S1 to S5
References (31–34)

10 April 2016; accepted 30 June 2016
10.1126/science.aaf8533

ELECTROCHEMISTRY

Nanostructured transition metal dichalcogenide electrocatalysts for CO₂ reduction in ionic liquid

Mohammad Asadi,¹ Kibum Kim,^{1,2*} Cong Liu,^{3*} Aditya Venkata Addepalli,¹ Pedram Abbasi,¹ Poya Yasaei,¹ Patrick Phillips,⁴ Amirhossein Behranginia,¹ José M. Cerrato,⁵ Richard Haasch,⁶ Peter Zapol,³ Bijandra Kumar,^{1,7} Robert F. Klie,⁴ Jeremiah Abiade,¹ Larry A. Curtiss,^{3†} Amin Salehi-Khojin^{1†}

Conversion of carbon dioxide (CO₂) into fuels is an attractive solution to many energy and environmental challenges. However, the chemical inertness of CO₂ renders many electrochemical and photochemical conversion processes inefficient. We report a transition metal dichalcogenide nanoarchitecture for catalytic electrochemical CO₂ conversion to carbon monoxide (CO) in an ionic liquid. We found that tungsten diselenide nanoflakes show a current density of 18.95 milliamperes per square centimeter, CO faradaic efficiency of 24%, and CO formation turnover frequency of 0.28 per second at a low overpotential of 54 millivolts. We also applied this catalyst in a light-harvesting artificial leaf platform that concurrently oxidized water in the absence of any external potential.

Electrochemical or photochemical reduction of carbon dioxide (CO₂) could in principle conveniently recycle the greenhouse gas back into fuels (1–6). However, existing catalysts are too inefficient in practice (7–11): Either weak binding interactions between the reaction intermediates and the catalyst give rise to high overpotentials, or slow electron transfer kinetics result in low exchange current densities. Both of these metrics depend not only on the intrinsic electronic properties of the catalyst, but also on the solvent and the catalyst morphology. Recently, we reported that three-dimensional (3D) bulk molybdenum disulfide (MoS₂) catalyzes CO₂ reduction to CO at an extremely low overpotential (54 mV) (12) in an ionic liquid (IL). Here, we report 2D nanoflake (NF) architectures of this and other transition metal dichalcogenides (TMDCs) that manifest much higher performance for electrocatalytic CO₂ reduction in the IL 1-ethyl-3-methylimidazolium tetrafluoroborate (EMIM-BF₄).

CO₂ reduction activities of similarly sized (~100 nm) TMDC NFs including MoS₂, WS₂, MoSe₂, and WSe₂ were tested using a rotating disc electrode. All TMDCs were grown using a chemical vapor transport technique (13). Figure 1A shows cyclic voltammetry (CV) results of WSe₂ NFs, and bulk MoS₂ as well as Ag nanoparticles (Ag NPs) and bulk Ag as a representative noble-metal catalyst. All experiments were performed inside a two-compartment, three-electrode electrochemical cell (fig. S6) using an electrolyte of 50 volume percent (vol %) EMIM-BF₄ and 50 vol % deionized water; this composition gives the maximum CO₂ reduction activity (13). The polarization curves of all studied catalysts were obtained by sweeping potential between +0.8 and -0.764 V versus RHE (reversible hydrogen electrode; all potentials reported here are based on RHE) with a scan rate of 50 mV s⁻¹ (Fig. 1A and fig. S8). We also performed chronoamperometry at different applied potentials for WSe₂ NFs. The results indicate that the obtained current densities for all applied potentials are 10 to 20% less than the CV results with 50 mV/s scan rate (fig. S9). The difference is attributed to the charging current (capacitive behavior) in the CV measurements.

The CO₂ reduction began at -0.164 V (overpotential of 54 mV) for WSe₂ NFs, as confirmed by faradaic efficiency (FE) measurements (Fig. 1B). At this potential (overpotential of 54 mV), a current density of 18.95 mA/cm² (normalized on the basis of geometrical surface area) was ob-

tained for WSe₂ NFs; by comparison, current densities were 0.19 mA/cm² for bulk Ag, 1.57 mA/cm² for Ag NPs, and 3.4 mA/cm² for bulk MoS₂. The CO formation FEs for WSe₂ NFs (Fig. 1B) and bulk MoS₂ (12) were 24% and 3%, respectively. However, the Ag NPs and bulk Ag did not reduce CO₂ at this overpotential. At -0.764 V potential, the recorded current density for WSe₂ NFs was 330 mA cm⁻², versus 3.3 mA cm⁻² for bulk Ag, 11 mA cm⁻² for Ag NPs, and 65 mA cm⁻² for bulk MoS₂. The CO formation turnover frequency (TOF) (Fig. 1C) (13), a measure of per-site activity of catalysts to produce CO, was 0.28 s⁻¹ for WSe₂ NFs versus 0.016 s⁻¹ for bulk MoS₂. However, this value was zero for Ag NPs, as they could not produce CO at this overpotential (54 mV). Figure 1C also shows that the CO formation TOF of WSe₂ was approximately three orders of magnitude higher than that of Ag NPs in the overpotential range of 150 to 650 mV.

Gas chromatography and differential electrochemical mass spectroscopy analyses indicated that CO and H₂ were the only gas-phase products (5, 11, 12, 14–16) in the potential range of 0 to -0.764 V (13). The measured FE for WSe₂ NFs/IL (Fig. 1B) showed that this system is highly selective for CO formation at high potentials (-0.2 to -0.764 V). However, at smaller potentials (-0.164 to -0.2 V), it produces a mixture of CO and H₂ (synthesis gas). Figure S13 shows the selectivity (FE) results of all TMDCs tested in this study (13).

The catalytic performance of TMDC NFs was compared with that of other reported catalysts (Fig. 1D) by multiplying current density (activity) by CO formation FE (selectivity). At 100 mV overpotential, the performance of WSe₂ NFs exceeded that of bulk MoS₂ and Ag NPs tested under identical conditions in an ionic liquid by a factor of nearly 60. The performance of WSe₂ NFs also exceeds those of Au NPs (17) and Cu NPs (18) by three orders of magnitude. Additionally, at this overpotential, the performance of WSe₂ exceeded that of WS₂ and MoSe₂ NFs by factors of 3 and 2, respectively (Fig. 1D). We also performed chronoamperometry experiments to examine the electrochemical stability of WSe₂ NFs in 50:50 vol % IL/deionized water. At the applied potential of -0.364 V (0.254 V overpotential), a small decay (10%) was observed after 27 hours of continuous operation of the three-electrode two-compartment cell (fig. S14) (13).

The photochemical performance of WSe₂/IL was also studied using a custom-built wireless setup. This artificial leaf mimics the photosynthesis process in the absence of any external applied potential. The cell (Fig. 2A) (13) is composed of three major segments: (i) two amorphous silicon triple-junction photovoltaic (PV-a-si-3jn) cells in series to harvest light, (ii) the WSe₂/IL cocatalyst

¹Department of Mechanical and Industrial Engineering, University of Illinois, Chicago, IL 60607, USA. ²Department of Mechanical Engineering, Chungbuk National University, Cheongju 361-763, South Korea. ³Materials Science Division, Argonne National Laboratory, Argonne, IL 60439, USA. ⁴Department of Physics, University of Illinois at Chicago, Chicago, IL 60607, USA. ⁵Department of Civil Engineering, University of New Mexico, Albuquerque, NM 87131, USA. ⁶Materials Research Laboratory, University of Illinois at Urbana-Champaign, Urbana, IL 61801, USA. ⁷Conn Center for Renewable Energy Research, University of Louisville, Louisville, KY 40292, USA.

*These authors equally contributed to this work. †Corresponding author. Email: salehikh@uic.edu (A.S.-K.); curtiss@anl.gov (L.A.C.)

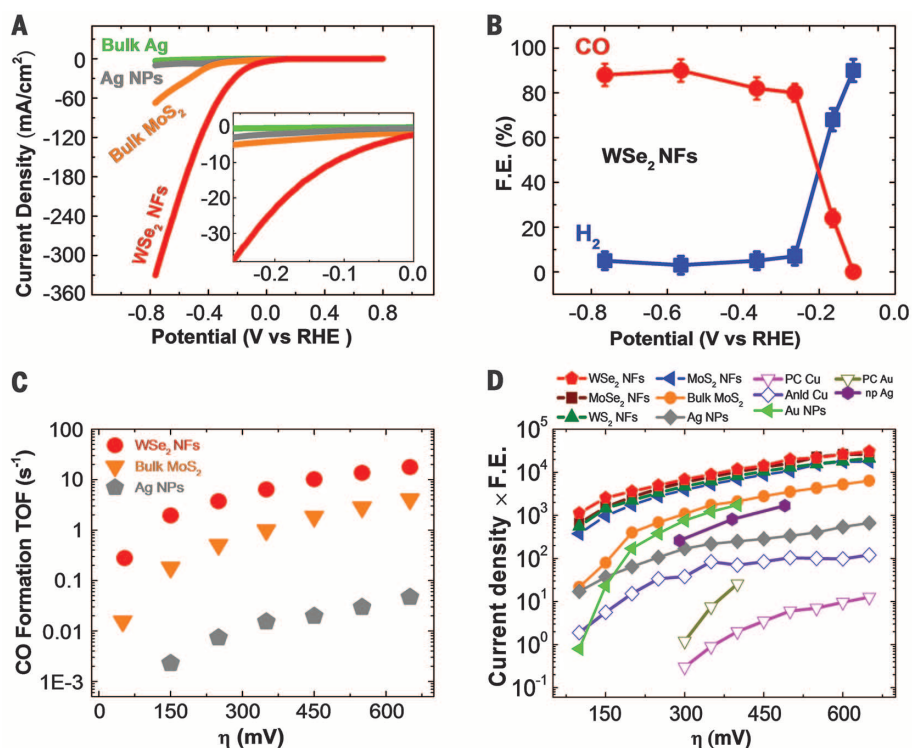


Fig. 1. CO₂ reduction performance of the TMDC catalysts, Ag NPs, and bulk Ag in the EMIM-BF₄ solution. (A) Cyclic voltammetry (CV) curves for WSe₂ NFs, bulk MoS₂, Ag nanoparticles (Ag NPs), and bulk Ag in CO₂ environment. Inset shows the current densities in low overpotentials. (B) CO and H₂ overall faradaic efficiency (FE) at different applied potentials for WSe₂ NFs. The error bars represent SD of four measurements. (C) CO formation TOF of WSe₂ NFs, bulk MoS₂, and Ag NPs in IL electrolyte at overpotentials of 54 to 650 mV. At 54 mV overpotential, Ag NPs' result is zero. (D) Overview of different catalysts' performance at different overpotentials (η). All TMDC and Ag NP data were obtained from chronoamperometry experiments under identical conditions. Data for other catalysts are from (12).

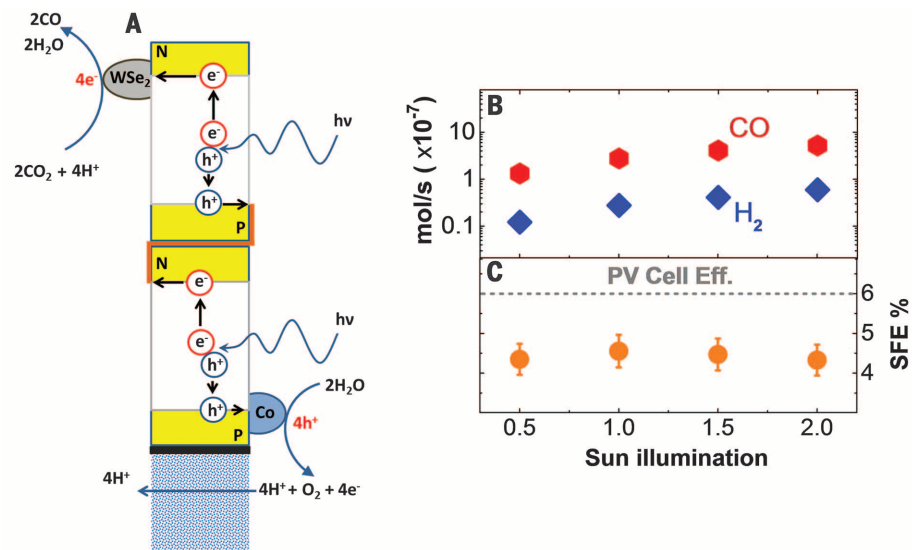


Fig. 2. Artificial leaf. (A) Schematic of the cell design. (B) Rate of product formation (mol/s) with respect to different Sun illuminations. (C) Calculated solar-to-fuel efficiency (SFE) of photochemical process using the WSe₂/IL cocatalyst system. Our calculation indicates ~4.6% SFE, which is limited by the maximum efficiency of PV-a-si-3jn (~6.0%). Error bars indicate uncertainty in the calculated SFE (table S5) (13).

system on the cathode side for CO₂ reduction, and (iii) cobalt (Co^{II}) oxide/hydroxide in potassium phosphate pH = 7.0 (KPi) electrolyte on the anode side to catalyze the oxygen evolution reaction (19–21). Because the CO₂ reduction and oxygen evolution reactions in the artificial leaf system are electrically coupled together through the photovoltaic, the production and consumption rates of electrons and protons are equal on the anode and cathode sides of the cell. When the reaction starts, proton (H⁺) generation is initiated in the KPi solution (anode side) through the oxygen evolution reaction (decreasing the initial pH of 7); on the IL electrolyte (cathode side), the CO₂ reduction reaction consumes H⁺ available in the IL electrolyte (increasing the initial pH of ~3.2). During this transient period, diffusion of the K⁺ ions through the proton exchange membrane from the anode to the cathode side compensates the charge imbalance to achieve charge neutrality (fig. S17) (13). However, after this period (~5 min), the pH in the KPi solution and the IL approaches ~3.4, where the operation of the artificial leaf system reaches steady state and H⁺ diffuses in place of K⁺. Our measurements indicate that 1.43×10^{-4} M K⁺ diffuses to the IL in the transient stage and that its concentration remains constant under steady-state operation. This quantification is consistent with the change in the H⁺ concentration (1.52×10^{-4} M) on the cathode side. The PV-a-si-3jn cell can function continuously for 5 hours (fig. S18) before corrosion of the transparent indium tin oxide layer on the anode inhibits operation (fig. S19) (13). However, replacing the PV-a-si-3jn cells restores performance to its previous level.

To test the stability of ionic liquid (50 vol % EMIM-BF₄ in water) and KPi electrolytes, we replaced the PV-a-si-3jn cells every 4 hours for a cumulative time of 100 hours. Results shown in table S3 (13) indicate that, within error margins, the same molar quantities of CO and H₂ were produced during each 4-hour period of the 100-hour-long operation of the artificial leaf, confirming the durability of both anode (KPi) and cathode (50/50 vol% IL/water) electrolytes. We also observed no significant change in the pH of the solution after 100 hours (13). Moreover, our calculations (13) indicate that a negligible amount of water (~0.018 ml/hour) is produced during the CO₂ reduction reaction on the cathode side relative to the total volume of electrolyte (100 ml of IL/water) used in our experiment.

Figure 2B shows the molar rates of product formation with respect to simulated solar illumination (number of Suns). The respective yields of CO and H₂ measured by GC follow an approximately 10:1 ratio for the entire range of illuminations. This result is consistent with our FE measurements obtained at higher overpotentials in the three-electrode electrochemical setup. We also calculated the solar-to-fuel conversion efficiency (SFE) for our photochemical process (Fig. 2C), obtaining a value of ~4.6% limited by the maximum efficiency of the PV-a-si-3jn cell (~6.0%) (13, 20). This SFE is higher than that of

the water-splitting reaction (~2.5%) previously measured using an identical triple-junction photovoltaic (PV-a-si-3jn) cell (20). Our measurements indicate that the SFE of the system remains stable for 5 hours of continuous operation (fig. S20) (I3). The SFEs of the artificial leaf during 100 hours of operation (with successive PV-a-si-3jn replacements) are shown in table S6.

Next, we performed electrochemical impedance spectroscopy (EIS) at 150 mV overpotential to measure the charge transfer resistance (R_{ct}) for WSe₂ NFs, bulk MoS₂, and Ag NPs catalysts (I3, 22–24). A charge transfer resistance is correlated to the number of electrons transferred from the catalyst surface to the reactant (25–27) as well as intermediate formation inside the double layer (22, 23). Our experimental results (Fig. 3) indicate that the R_{ct} of WSe₂ is ~180 ohms, versus ~420 ohms for bulk MoS₂ and ~550 ohms for Ag NPs.

Additionally, we measured the work function of WSe₂ and the other TMDCs by ultraviolet

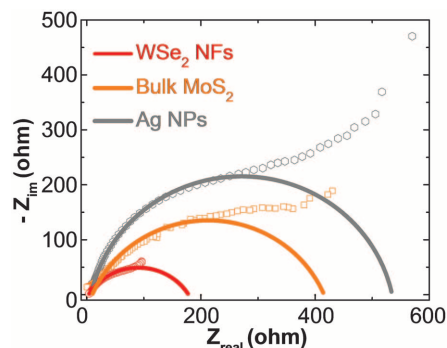


Fig. 3. Electrochemical impedance spectroscopy of CO₂ reduction using WSe₂ NFs, bulk MoS₂, and Ag NPs at 150 mV overpotential.

photoelectron spectroscopy (UPS) (I1, I3) (fig. S22). Our results indicate a considerably lower work function of WSe₂ NFs (3.52 eV) compared to bulk MoS₂ (3.99 eV) (I2) and Ag NPs (4.38 eV), confirming the EIS data. These results provide evidence that the superior electronic properties of W edge atoms result in a faster electron transfer and consequently higher catalytic activity during CO₂ reduction.

To characterize the atomic arrangement of edge atoms, we performed scanning transmission electron microscopy (STEM) analysis on several liquid-exfoliated monolayers and multiple layers of WSe₂ NFs (fig. S23A) (I3). The line intensity profile of single-layer WSe₂ NF (fig. S23B) indicates that the edges of the nanoflakes are W-terminated. Moreover, STEM analysis on the edge atoms after 27 hours of chronoamperometry (fig. S14) indicates a stable atomic structure of W edge sites (fig. S23, C and D). These results suggest that transition metals with d-orbital electrons on the edge sites mainly contribute to the CO₂ reduction without any evidence of instability over time. X-ray photoelectron spectroscopy data further verified the long-term stability of the catalyst (fig. S24, A to D) (I2, I3).

Density functional theory (DFT) calculations were performed to gain insight into the catalytic properties of the TMDC NFs (I3). The calculated reaction free energies of the CO₂ → CO pathway using a computational hydrogen electron approach at zero potential (28) show that the formation of COOH* is highly endergonic and is the rate-limiting step for both Ag(111) and the Ag₅₅ cluster (Fig. 4A). The Ag₅₅ cluster requires less energy than Ag(111) to form COOH* because of the presence of undercoordinated Ag atoms of the cluster. This result explains the lower overpotential of Ag nanoparticles relative to bulk Ag, in agreement with other studies (7). COOH* formation is sim-

ilarly endergonic on other metal surfaces such as Pd, Au, and Cu (7, 29, 30). However, on the metallic edges of the TMDC NFs, COOH* formation is exergonic because of strong binding to the TMDC metal edge sites. The CO* is also much more stable on the TMDC NFs than on Ag, residing at lower energy than COOH*. This energetic ordering suggests that the formation of CO* from CO₂ is kinetically more favorable on the TMDC NFs than on Ag (Fig. 4A) resulting in lower overpotentials. In addition, the calculated projected density of states of the edge metal atom (Mo or W) reveals that the d-band centers of these metal edges (Fig. 4, B and C, and fig. S26, A to D) (I3) are much closer to the Fermi level than those of the Ag(111) surface, further supporting the strong binding interactions of the adsorbed intermediates with the TMDC NFs (31, 32). However, the strong binding of CO on the TMDCs also inhibits desorption of CO, which becomes the rate-limiting step in the TMDC systems. Previous studies have indicated that the coverage of the adsorbed intermediates significantly affects the binding energies (33, 34). We further investigated the effect of CO coverage on the metal edge of the TMDCs and found that each metal atom on the TMDC edge can bind up to two CO molecules ($\theta_{CO} \leq 2$ ML) (I3). The binding energy per CO on a metal atom (when $\theta_{CO} = 1$ ML) ranges from 0.8 to 1.1 eV (Fig. 4A), whereas the binding energy per second CO on a metal atom (when $\theta_{CO} = 2$ ML) decreases to 0.3 to 0.5 eV. This finding suggests that the metal edges of the TMDCs likely have high CO coverage ($\theta_{CO} > 1$ ML) during the catalytic reaction to maintain a high turnover rate.

We also calculated the work functions of the monolayers of the four TMDCs (fig. S27). Our calculations show a trend of MoS₂ > WS₂ > MoSe₂ > WSe₂, consistent with experimental measurements of the work functions (fig. S22) (I3). This trend of work functions correlates with the trend of the experimental activities as measured by current densities of the four TMDCs, suggesting that the electron transfer properties of the TMDCs play an important role in the electrochemical reduction of CO₂. In this case, WSe₂ has the lowest work function and is the best TMDC for CO₂ activation among the tested materials.

The ionic liquid also plays an important role in the CO₂ electrochemical reduction. Our previous study suggested that the EMIM⁺ ion helps transport CO₂ to the catalyst surface by complexation under acidic conditions (I2). Overall, we attribute the exceptional performance of the present catalysts to a combination of low overpotentials and efficient electron transfer properties of the TMDC NFs and the IL-enhanced local CO₂ concentration.

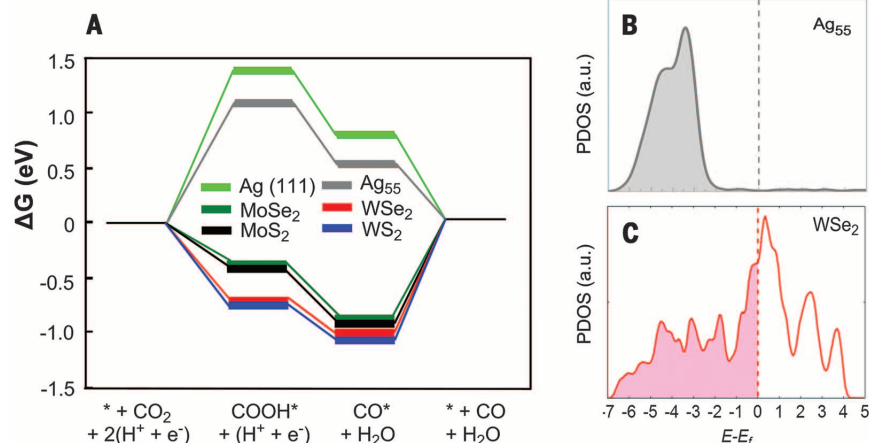


Fig. 4. Density functional theory analysis. (A) Calculated free energy diagrams for CO₂ electroreduction to CO on Ag(111), Ag₅₅ NPs, MoS₂, WS₂, MoSe₂, and WSe₂ NFs at 0 V RHE. **(B)** Calculated partial density of states of the d band (spin-up) of the surface Ag atom of Ag₅₅. **(C)** Calculated partial density of states of the surface bare metal edge atom (W) of the WSe₂ NFs. The calculations of the Ag systems are at CO coverage of 1/16 ML; those of the TMDC systems are at CO coverage of 1 ML. See (I3) for details of the coverage effects in the TMDC systems.

REFERENCES AND NOTES

- R. Angamuthu, P. Byers, M. Lutz, A. L. Spek, E. Bouwman, *Science* **327**, 313–315 (2010).
- J. Hawecker, J.-M. Lehn, R. Ziessel, *Helv. Chim. Acta* **69**, 1990–2012 (1986).
- J. Medina-Ramos, J. L. DiMeglio, J. Rosenthal, *J. Am. Chem. Soc.* **136**, 8361–8367 (2014).

4. R. D. Richardson, E. J. Holland, B. K. Carpenter, *Nat. Chem.* **3**, 301–303 (2011).
5. B. A. Rosen *et al.*, *Science* **334**, 643–644 (2011).
6. L. Zhang, D. Zhu, G. M. Nathanson, R. J. Hamers, *Angew. Chem. Int. Ed.* **53**, 9746–9750 (2014).
7. D. Gao *et al.*, *J. Am. Chem. Soc.* **137**, 4288–4291 (2015).
8. H. Mistry *et al.*, *J. Am. Chem. Soc.* **136**, 16473–16476 (2014).
9. R. Reske, H. Mistry, F. Beharfarid, B. Roldan Cuenya, P. Strasser, *J. Am. Chem. Soc.* **136**, 6978–6986 (2014).
10. W. Zhu *et al.*, *J. Am. Chem. Soc.* **135**, 16833–16836 (2013).
11. A. Salehi-Khojin *et al.*, *J. Phys. Chem. C* **117**, 1627–1632 (2013).
12. M. Asadi *et al.*, *Nat. Commun.* **5**, 4470 (2014).
13. See supplementary materials on Science Online.
14. J. L. DiMeglio, J. Rosenthal, *J. Am. Chem. Soc.* **135**, 8798–8801 (2013).
15. B. Kumar *et al.*, *Nat. Commun.* **4**, 2819 (2013).
16. B. A. Rosen, W. Zhu, G. Kaul, A. Salehi-Khojin, R. I. Masel, *J. Electrochem. Soc.* **160**, H138–H141 (2012).
17. Y. Chen, C. W. Li, M. W. Kanan, *J. Am. Chem. Soc.* **134**, 19969–19972 (2012).
18. C. W. Li, M. W. Kanan, *J. Am. Chem. Soc.* **134**, 7231–7234 (2012).
19. D. A. Lutterman, Y. Surendranath, D. G. Nocera, *J. Am. Chem. Soc.* **131**, 3838–3839 (2009).
20. S. Y. Reece *et al.*, *Science* **334**, 645–648 (2011).
21. M. W. Kanan, D. G. Nocera, *Science* **321**, 1072–1075 (2008).
22. Y. Tan *et al.*, *Adv. Mater.* **26**, 8023–8028 (2014).
23. D. J. Li *et al.*, *Nano Lett.* **14**, 1228–1233 (2014).
24. J. Kibsgaard, Z. Chen, B. N. Reinecke, T. F. Jaramillo, *Nat. Mater.* **11**, 963–969 (2012).
25. G. Fishman, D. Calecki, *Phys. Rev. Lett.* **62**, 1302–1305 (1989).
26. T. Fujita *et al.*, *Phys. Rev. Lett.* **101**, 166601 (2008).
27. C. Gong *et al.*, *ACS Nano* **7**, 11350–11357 (2013).
28. J. K. Nørskov *et al.*, *J. Phys. Chem. B* **108**, 17886–17892 (2004).
29. H. A. Hansen, J. B. Varley, A. A. Peterson, J. K. Nørskov, *J. Phys. Chem. Lett.* **4**, 388–392 (2013).
30. A. A. Peterson *et al.*, *Energy Environ. Sci.* **3**, 1311 (2010).
31. B. Hammer, J. K. Nørskov, *Adv. Catal.* **45**, 71–129 (2000).
32. B. Hammer, J. K. Nørskov, *Nature* **376**, 238–240 (1995).
33. C. Tsai, F. Abild-Pedersen, J. K. Nørskov, *Nano Lett.* **14**, 1381–1387 (2014).
34. C. Tsai, K. Chan, F. Abild-Pedersen, J. K. Nørskov, *Phys. Chem. Chem. Phys.* **16**, 13156–13164 (2014).

ACKNOWLEDGMENTS

Supported by NSF grant CBET-1512647 (A.S.-K.); the MRSEC Materials Preparation and Measurement Laboratory shared user facility at the University of Chicago (grant NSF-DMR-1420709); the EPIC facility (NUANCE Center–Northwestern University), which has received support from the MRSEC program (grant NSF-DMR-1121262) at the Materials Research Center; the Nanoscale Science and Engineering Center (NSF EEC-0647560) at the International Institute for Nanotechnology; and the State of Illinois through the International Institute for Nanotechnology. The work at Argonne National Laboratory was supported by the U.S. Department of Energy under contract DE-AC0206CH11357 from the Division of Materials Science and Engineering, Basic Energy Science (P.Z., C.L., and L.A.C.). The authors also acknowledge Analytical Chemistry Laboratory of the Earth and Planetary Sciences Department, University of New Mexico. Author contributions: A.S.-K., M.A., and B.K. conceived the idea; A.S.-K., M.A., K.K., and A.V.A. performed the electrochemical experiments; M.A., P.A., and A.B. grew and synthesized the TMDC flakes; M.A., B.K., and P.Y. did the characterizations; C.L., P.Z., and L.C. performed DFT calculations; P.P. and R.K. carried out STEM and electron energy loss spectroscopy; R.H. performed UPS experiments; J.M.C. performed elemental analysis measurement; J.A. and A.S.K. jointly supervised M.A.'s efforts; and all authors contributed to the manuscript before submission. A.S.-K., M.A., and B.K. have filed a provisional patent application. The other authors declare no competing financial interests.

SUPPLEMENTARY MATERIALS

www.sciencemag.org/content/353/6298/467/suppl/DC1
Materials and Methods
Figs. S1 to S27
Tables S1 to S7
References (35–53)

14 February 2016; accepted 1 July 2016
10.1126/science.aaf4767

PALEOCEANOGRAPHY

North Atlantic ocean circulation and abrupt climate change during the last glaciation

L. G. Henry,^{1*} J. F. McManus,¹ W. B. Curry,^{2,3} N. L. Roberts,⁴
A. M. Piotrowski,⁴ L. D. Keigwin²

The most recent ice age was characterized by rapid and hemispherically asynchronous climate oscillations, whose origin remains unresolved. Variations in oceanic meridional heat transport may contribute to these repeated climate changes, which were most pronounced during marine isotope stage 3, the glacial interval 25 thousand to 60 thousand years ago. We examined climate and ocean circulation proxies throughout this interval at high resolution in a deep North Atlantic sediment core, combining the kinematic tracer protactinium/thorium (Pa/Th) with the deep water-mass tracer, epibenthic $\delta^{13}\text{C}$. These indicators suggest reduced Atlantic overturning circulation during every cool northern stadial, with the greatest reductions during episodic Hudson Strait iceberg discharges, while sharp northern warming followed reinvigorated overturning. These results provide direct evidence for the ocean's persistent, central role in abrupt glacial climate change.

Unlike the relatively stable preindustrial climate of the past 10 thousand years, glacial climate was characterized by repeated millennial oscillations (1). These alternating cold stadial and warm interstadial events were most abrupt and pronounced on Greenland and across much of the northern hemisphere, with the most extreme regional conditions during several Heinrich (H) events (2), catastrophic iceberg discharges into the subpolar North Atlantic Ocean. These abrupt events not only had an impact on global climate but also are associated with widespread reorganizations of the planet's ecosystems (3). Geochemical fingerprinting of the ice-rafted detritus (IRD) associated with the most pronounced of these events consistently indicates a source in the Hudson Strait (HS) (4), so we abbreviate this subset of H events as HS events and their following cool periods as HS stadials. During northern stadials, ice cores show that Antarctica warmed, and each subsequent rapid northern hemisphere warming was followed shortly by cooling at high southern latitudes (5). Explanations for the rapidity and asynchrony of these climate changes require a mechanism for partitioning heat on a planetary scale, initiated either through reorganization of atmospheric structure (6) or the ocean's thermohaline circulation, particularly the Atlantic meridional overturning circulation (AMOC) (7–10). Coupled climate models have successfully used each of these mechanisms to generate time series that replicate climate variability observed in paleoclimate archives (9, 11). We investigated the relationship between Northern Hemispheric cli-

mate as recorded in Greenland ice cores and marine sediments, along with isotopic deep-sea paleoproxies sensitive to changes in North Atlantic Deep Water (NADW) production and AMOC transport during marine isotope stage three (MIS3). Throughout that time, when global climate was neither as warm as today nor as cold as the last glacial maximum (LGM), ice sheets of intermediate size blanketed much of the northern hemisphere, and large millennial stadial-interstadial climate swings (6, 8) provide a wide dynamic range that allows examination of the ocean's role in abrupt change.

Sediment samples were taken from the long (35 m) core KNR191-CDH19—recovered from the Bermuda Rise (33° 41.443' N; 57° 34.559' W, 4541 m water depth) in the northwestern Atlantic Ocean (Fig. 1), near previous seafloor sampling at Integrated Ocean Drilling Program (IODP) site 1063—and coring sites KNR31 GPC-5, EN120 GGC-1, MD95-2036, OCE326-GGC5, and others. Because this region of the deep North Atlantic is characterized by steep lateral gradients in tracers of NADW and Antarctic Bottom Water (AABW), the Bermuda Rise has been intensively used to explore the connection between changes in ocean circulation and climate (7, 12). In this study, we measured the radioisotopes ^{231}Pa and ^{230}Th in bulk sediment, age-corrected to the time of deposition, along with stable carbon ($\delta^{13}\text{C}$) and oxygen ($\delta^{18}\text{O}$) isotope ratios in the microfossil shells of both epibenthic foraminifera (*Cibicides wuellerstorfi* and *Nuttallides umbonifera*) and planktonic foraminifera (*Globigerinoides ruber*), respectively, yielding inferences on relative residence times and the origin of deep water masses on centennial time scales.

Isotopes of protactinium and thorium, ^{231}Pa and ^{230}Th , are produced from the decay of ^{235}U and ^{234}U , respectively, dissolved in seawater. This activity of ^{231}Pa and ^{230}Th in excess of the amount

¹Lamont-Doherty Earth Observatory (LDEO), Columbia University, Palisades, NY 10964, USA. ²Woods Hole Oceanographic Institution, Woods Hole, MA 02543, USA.

³Bermuda Institute of Ocean Sciences, St. George's, Bermuda. ⁴University of Cambridge, Department of Earth Sciences, Cambridge CB2 3EQ, UK.

*Corresponding author. Email: lhenry@ldeo.columbia.edu

Nanostructured transition metal dichalcogenide electrocatalysts for CO reduction in ionic liquid

Mohammad AsadiKibum KimCong LiuAditya Venkata AddepalliPedram AbbasiPoya YasaeiPatrick PhillipsAmirhossein BehranginiaJosé M. CerratoRichard HaaschPeter ZapolBijandra KumarRobert F. KlieJeremiah AbiadeLarry A. CurtissAmin Salehi-Khojin

Science, 353 (6298), • DOI: 10.1126/science.aaf4767

Small and salty CO reduction scheme

Most artificial photosynthesis approaches focus on making hydrogen. Modifying CO, as plants and microbes do, is more chemically complex. Asadi *et al.* report that fashioning WSe and related electrochemical catalysts into nanometer-scale flakes greatly improves their activity for the reduction of CO to CO. An ionic liquid reaction medium further enhances efficiency. An artificial leaf with WSe reduced CO on one side while a cobalt catalyst oxidized water on the other side.

Science, this issue p. 467

View the article online

<https://www.science.org/doi/10.1126/science.aaf4767>

Permissions

<https://www.science.org/help/reprints-and-permissions>

Use of think article is subject to the [Terms of service](#)